RSC Advances

PAPER

View Article Online
View Journal | View Issue

Check for updates

Cite this: *RSC Adv.*, 2020, **10**, 17293

Fabrication of a magnetic ternary $ZnFe_2O_4/TiO_2$/RGO Z-scheme system with efficient photocatalytic activity and easy recyclability†

Yuwei Sun, [ab] Jiashuang Lei,[b] Yizhu Wang,[b] Qian Tang[b] and Chunli Kang *[a]

A magnetic composite based on TiO_2 nanosheets, $ZnFe_2O_4$ and reduced graphene oxide (RGO) was synthesized by a one-step hydrothermal synthesis method, which possessed the band structure of a Z-scheme photocatalytic system. The properties and structures of the samples were characterized by XRD, UV-Vis DRS, Raman spectroscopy, SEM, EDS, XPS and PL spectroscopy. Compared with TiO_2 nanosheets and the TiO_2/RGO composite, the obtained ternary composite with 3 wt% RGO exhibited a significant enhancement in photocatalytic activities, attributed to the efficient charge separation induced by the fabricated Z-scheme system. About 99.7% of *p*-nitrophenol (*p*-NP) degraded within 60 min under simulated solar irradiation. Trapping experiments showed that superoxide anions ($^{\bullet}O_2^-$) and hydroxyl radicals ($^{\bullet}OH$) were the main active species in the *p*-NP photocatalytic degradation. Finally, a possible photocatalytic mechanism of Z-scheme $ZnFe_2O_4/TiO_2$/RGO was proposed based on the results of trapping experiments and the energy bands of TiO_2 and $ZnFe_2O_4$.

Received 27th February 2020
Accepted 16th April 2020

DOI: 10.1039/d0ra01880e

rsc.li/rsc-advances

Open Access Article. Published on 05 May 2020. Downloaded on 2/8/2026 9:49:05 PM.
This article is licensed under a Creative Commons Attribution-NonCommercial 3.0 Unported Licence.

1. Introduction

Para-nitrophenol (*p*-NP), as an organic pollutant, is frequently used to produce pesticides, dyes and other chemicals.[1] It is considered a toxic organic pollutant when the concentration of *p*-NP exceeds 20 ppb in water.[2] Unfortunately, *p*-NP is hard to degrade using traditional biochemical treatments and the intermediates produced during treatment may maintain toxicity.[3,4] Photocatalytic oxidation technology has been considered to be an effective route because of its strong mineralization ability, lack of secondary pollutants and flexible operation.[5,6]

TiO_2 nanomaterials is a kind of widely used photocatalyst to degrade organic pollutants, due to its good stability, low price and high photocatalytic efficiency.[7,8] However, TiO_2 with high band gap energy (3.0–3.2 eV) can only use the narrow ultraviolet region of sunlight, which limits its practical application.[9,10] In general, there are two strategies to overcome this problem. One strategy is to regulate the crystal phase structure or morphology of TiO_2. Compared with ordinary TiO_2 or P25, TiO_2 nanosheets with high exposure (001) facets exhibit better performance in photocatalytic oxidation and reduction.[11] The other strategy is to composite with carbon materials.[12–15] Graphene with a 2D structure and excellent conductivity, always act as electron acceptors in photocatalytic reactions in order to increase the separation rate of photogenerated e^- and h^+ pairs.[16–18] It has been already proven that combination of TiO_2 and graphene can reduce the band gap energy and improve the photocatalytic efficiency.[19,20] Furthermore, Z-scheme systems are considered as very promising strategies to improve the photocatalytic degradation activity, in which photogenerated e^- and h^+ can be effectively separated.[21]

Unfortunately, TiO_2 and graphene composites are mostly in powder forms, which are not conducive to recovery from sewage. The introduction of magnetic materials into composite so that the new formed materials are magnetic and can be separated under the action of external magnetic force is considered to be an effective method for separating photocatalysts.[22] Accordingly, magnetic $ZnFe_2O_4$ with narrow bandgap energy (1.90 eV) has received extensive attention in the field of photocatalysis.[23,24] Zhu *et al.* studied a magnetic separable $ZnFe_2O_4/TiO_2$ composite, which exhibited an improved photocatalytic degradation.[25] The MB photodegradation rate was 93.2%.

In this work, the $ZnFe_2O_4/TiO_2$/RGO Z-scheme system was prepared by one step hydrothermal method and investigated for removal of *p*-NP solution. The phase composition and morphology of prepared composites were studied by XRD, Raman, UV-Vis DRS, PL, XPS and SEM and EDS analysis in details, the mass fraction of RGO in the ternary composite was optimized. The stability and reusability of the $ZnFe_2O_4/TiO_2$/RGO Z-scheme were measured by 5 times cycles of photocatalytic experiments. The possible removal mechanism of *p*-NP

[a]*Key Lab of Groundwater Resources and Environment, Ministry of Education, Jilin University, Changchun 130012, Jilin, China. E-mail: kangcl@jlu.edu.cn*

[b]*College of Environmental Science and Engineering, Jilin Normal University, Siping 136000, Jilin, China*

† Electronic supplementary information (ESI) available. See DOI: 10.1039/d0ra01880e

Open Access Article. Published on 05 May 2020. Downloaded on 2/8/2026 9:49:05 PM.
This article is licensed under a Creative Commons Attribution-NonCommercial 3.0 Unported Licence.

on the composites was provided based on the photocatalytic degradation experiments and the trapping experiments.

2. Experiments

2.1 Materials

Graphite powder was obtained from Alfa Aesar (the purity is over 99.8%). All chemicals used in the experiments were purchased from Sinopharm Chemical Reagent Co. Ltd., (Shanghai) and used without any further purification. Detailed calculation methods, active species trapping experiments and preparation of GO can be found in the ESI.†

2.1.1 Preparation of TiO_2 nanosheets. TiO_2 nanosheets were prepared by a hydrothermal method.[26] Concretely, 5.0 mL butyl titanate and 1 mL HF were dropped into 30 mL absolute ethylalcohol solution with stirring for 60 min. The above homogeneous solution was transferred into a Teflon-lined autoclave (50 mL) and kept it at 180 °C for 12 h. After the hydrothermal reaction, the white productions were washed with DI water and ethanol for several times, and then dried at 60 °C for one night.

2.1.2 Synthesis of $ZnFe_2O_4/TiO_2/RGO$ composites. The $ZnFe_2O_4/TiO_2/RGO$ composite was prepared by one-step hydrothermal method. Firstly, a certain mass of GO was dispersed in 10 mL DI water and 0.2 g TiO_2 nanosheets were dispersed in 10 mL ethanol by ultrasonication assistance, separately. After the 30 min, the two solutions of above were mixed and stirred for 0.5 h, which formed solution A. Secondly, 0.283 g $Zn(NO_3)_2 \cdot 6H_2O$ and 0.687 g $Fe(NO_3)_3 \cdot 9H_2O$ were added into 10 mL DI water and stirred for 0.5 h, which formed solution B. Thirdly, solution B was added to solution A, followed by addition of 1.5 g urea with intensively stirring for 2 h. Finally, mixed solution was placed into a Teflon-lined autoclave (50 mL) and maintained at 180 °C for 12 h. After completion of reaction, the brown precipitates were washed several times by DI water and ethanol and then dried at 60 °C for one night. When the $ZnFe_2O_4/TiO_2/RGO$ composite (ZTR) was prepared, 1 wt%, 3 wt% and 5 wt% of GO was added into solution A, and the obtained composites were denoted as ZTR 1, ZTR 3 and ZTR 5, respectively. For comparison, TiO_2/RGO composite (TR) and pure TiO_2 nanosheets were synthesized in the same condition (as seen in Scheme 1).

2.2 Instrumental measurements

The prepared composites were characterized by X-ray diffraction (XRD) (Rigaku D-max/3C) with Cu Kα radiation (40 kV and 200 mA, in the range of 5–80°). The SEM and EDS were measured by scanning electron microscopy (JEOL-JSM-6510) fitted out an energy disperse spectroscopy. The UV-Vis diffuse reflectance spectrum (UV-Vis DRS) were measured by spectrophotometer (Shimadzu UV-3600). The X-ray photoelectron spectroscopy (XPS) (ESCALAB 250XI) were tested with the binding energies at 284.6 eV from adventitious carbon referenced by C 1s line. The photoluminescence properties (PL) (Hitachi F4500) were operated by the photoluminescence detector with an excitation wavelength at 310 nm.

2.3 Photocatalytic efficiency evaluation

The photocatalytic efficiency of the prepared composites were evaluated by degradation of *p*-NP. Concretely, 20 mg photocatalyst was dispersed into *p*-NP solution (10 mg L^{-1}, 100 mL) with stirring for 0.5 h in dark to reach an adsorption–desorption equilibrium of *p*-NP on the photocatalyst. As a source of simulated solar irradiation, a 300 W xenon lamp was installed above the reactor. For comparison, we also tested the photocatalytic efficiency of the prepared composites in visible light irradiation. And the visible light irradiation source was the 300 W xenon lamp which installed filters to filter ultraviolet light (λ > 420 nm).

The concentration and total organic carbon (TOC) of *p*-NP were monitored by high performance liquid chromatography (HPLC, CTO-6A) and TOC analyzer (Analytic Jena, Germany), respectively. The photocatalytic data were averaged from three replicates experiments.

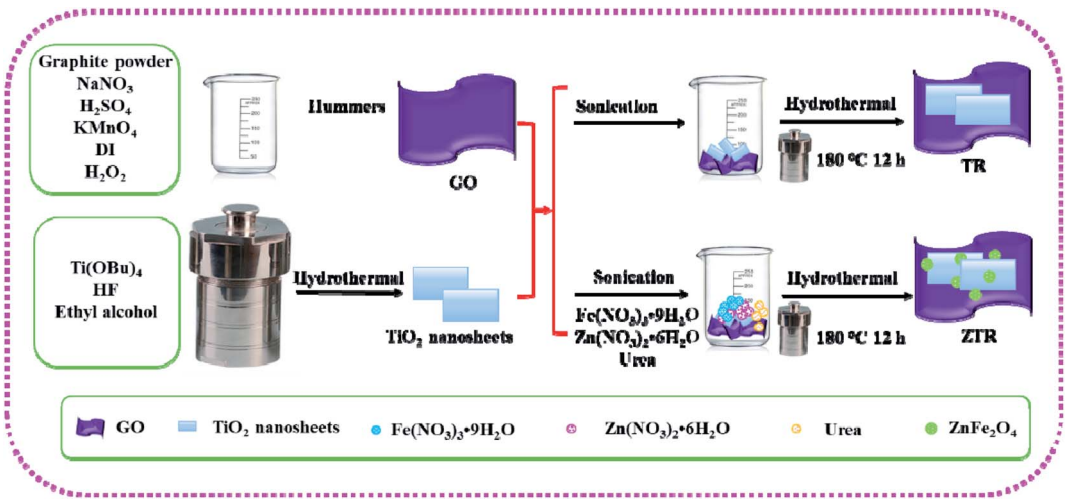

Scheme 1 Schematic diagram for synthesis of $ZnFe_2O_4/TiO_2$/RGO composite.

 This journal is © The Royal Society of Chemistry 2020

Open Access Article. Published on 05 May 2020. Downloaded on 2/8/2026 9:49:05 PM.
This article is licensed under a Creative Commons Attribution-NonCommercial 3.0 Unported Licence.

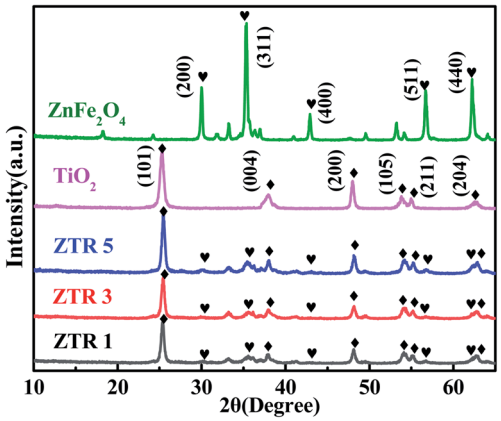

Fig. 1 XRD patterns of prepared composites.

Table 1 The band gap and photocatalytic activity of the samples[a]

Photocatalyst	E_g (eV)	k_1 (min^{-1})	k_2 (min^{-1})
$ZnFe_2O_4$	1.91	1.89×10^{-3}	1.52×10^{-3}
TiO_2	2.95	5.28×10^{-3}	2.16×10^{-3}
TR	2.87	12.89×10^{-3}	7.52×10^{-3}
ZTR 1	2.06	23.09×10^{-3}	12.78×10^{-3}
ZTR 3	1.94	36.85×10^{-3}	20.65×10^{-3}
ZTR 5	1.99	26.65×10^{-3}	15.11×10^{-3}

[a] k_1 is the first-order rate constant values under simulated solar irradiation. k_2 is the first-order rate constant values under visible light irradiation.

3. Results and discussion

3.1 Characterization of composites

Fig. 1 shows XRD patterns of $ZnFe_2O_4$, TiO_2 and ZTR 1, ZTR 3, ZTR 5 composites. The peaks of TiO_2 nanosheets are located at 2θ of 25.3°, 37.8°, 48°, 53.9°, 55.1° and 62.7°, corresponding to the (101), (004), (200), (105), (211) and (204) of anatase TiO_2 (JCPDS 21-1272), respectively. Compared to the peaks of TiO_2 nanosheets, there are new five diffraction peaks at 2θ of 29.9°, 35.3°, 42.8°, 56.6° and 62.4°, which corresponded to (220), (311), (400), (511) and (440) crystal planes of $ZnFe_2O_4$ (JCPDS 82-1049), respectively. The two sets of diffraction peaks of ZTR 1, ZTR 3 and ZTR 5 composites reveal that the $ZnFe_2O_4/TiO_2$/RGO composites were successfully synthesized. Notably, the diffraction peaks of RGO are not obvious, which maybe due to the low content of RGO.[27] Furthermore, we calculated the grain sizes of TiO_2 in ZTR 1, ZTR 3 and ZTR 5 composites by using the Scherrer equation ($D = K\lambda(B\cos\theta)^{-1}$). The grain sizes of TiO_2 in ZTR 1, ZTR 3 and ZTR 5 composites are 21.3, 20.2 and 19.8 nm, respectively. The grain sizes of TiO_2 decreased slightly with the increase of RGO content in the composite.

The UV-Vis diffuse reflectance spectra (UV-Vis DRS) was used to investigate the optical properties and energy band features of the composites. In Fig. 2a, TiO_2 nanosheets mainly respond to UV light and have absorption edge at about 400 nm. In addition, pure $ZnFe_2O_4$ displays a strong absorption in UV and visible regions, indicating $ZnFe_2O_4$ possesses excellent light absorption property. Compared with TiO_2 nanosheets, the optical response range of TR composite is enhanced in the visible light region, which may be attributed to electronic interactions between of TiO_2 and RGO.[28] Moreover, ZTR 1, ZTR 3 and ZTR 5 composites all have the higher absorbances from 350 nm to 560 nm than TiO_2 and TR, indicating a more efficient utilization of the solar light could be achieved in ZTR composites, because of the effective synergistic effects among TiO_2, $ZnFe_2O_4$ and RGO.[25,28] As illustrated in Fig. 2b and S2,† the band gap energies (E_g) of the prepared samples are listed in Table 1. The calculated E_{VB} and E_{CB} of TiO_2 are 2.785 eV and −0.165 eV, respectively. Correspondingly, the E_{VB} and E_{CB} of $ZnFe_2O_4$ are 1.505 eV and −0.405 eV, respectively. The details of the calculation are shown in the ESI.†

The morphologies of the composites were investigated using SEM microscopy. Fig. 3a shows the SEM image of TiO_2 nanosheets, in which TiO_2 is a sheet shaped structure with a uniform size. According to the symmetries, two flat and square surfaces in the crystal structure in TiO_2 nanosheets may be attributed to (001) facets.[29] As shown in Fig. 3b, RGO exhibits a radioactive folded morphology features after undergoing hydrothermal treatment. TiO_2 nanosheets distribute on the surface and fold of

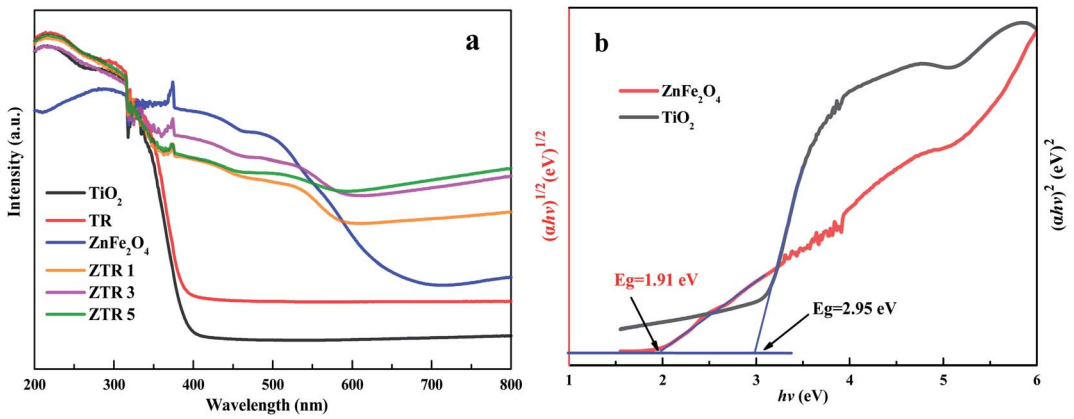

Fig. 2 (a) UV-Vis DRS spectrum of the prepared composites and (b) calculation on the band gap energies of $ZnFe_2O_4$ and TiO_2.

Open Access Article. Published on 05 May 2020. Downloaded on 2/8/2026 9:49:05 PM.
This article is licensed under a Creative Commons Attribution-NonCommercial 3.0 Unported Licence.

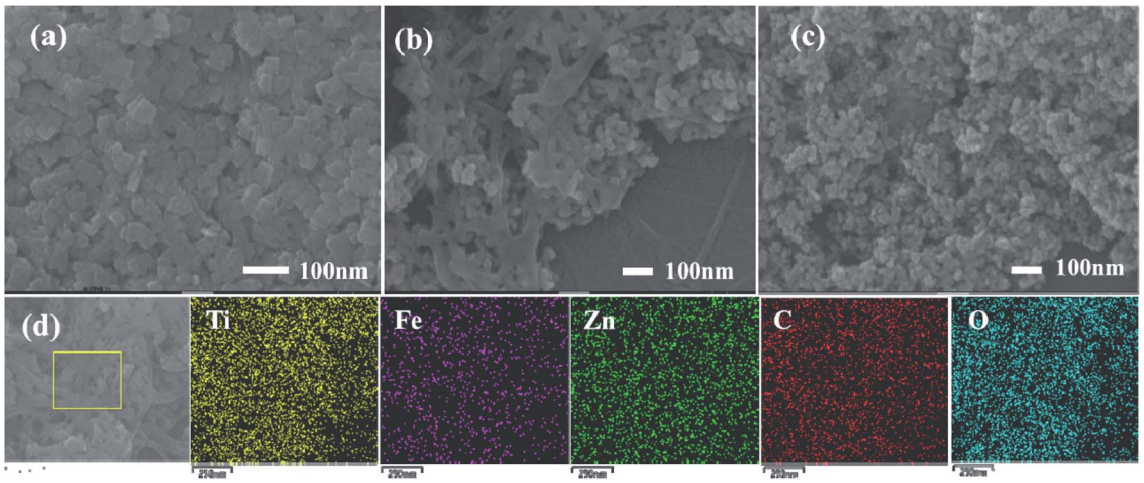

Fig. 3 SEM images of (a) TiO_2 nanosheets, (b) TR composite and (c) ZTR 3 composite.

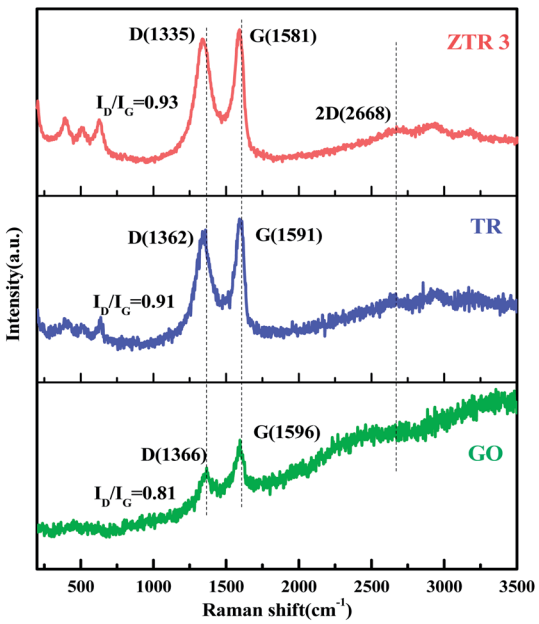

Fig. 4 Raman spectrum of GO, TR and ZTR 3 composites.

RGO. The SEM image of ZTR 3 composite shows in Fig. 3c, the existence of well dispersed TiO_2 nanosheets and $ZnFe_2O_4$ nanoparticles with uniform size on the surface and fold of RGO. Moreover, the element composition of ZTR 3 (Fig. 3d) composite was analyzed by energy dispersive X-ray spectroscopy (EDS). As shown in Fig. S3,† elements of C, O, Ti, Fe, Zn are detected in the ZTR 3 composite, which further confirms that the successful synthesis of the ternary composite.

Fig. 4 presents Raman scattering spectra of GO, TR and ZTR 3 composites. It shows two Raman peaks at 1366 and 1596 cm^{-1} for GO, which correspond to the positions of D and G bands, respectively. As for TR and ZTR 3 composites, several characteristic bands between 100–1000 cm^{-1} correspond to the TiO_2 and $ZnFe_2O_4$, respectively.[30,31] Notably, the redshift of G band from GO (1596 cm^{-1}) to TR (1591 cm^{-1}) and ZTR 3 (1581 cm^{-1}) can be considered as the reduction of GO to RGO after hydrothermal reaction. In addition, two-dimensional (2D) band at 2668 cm^{-1} and is also observed in ZTR 3 composites, indicating the presence of monolayer graphene.[32] In addition, the I_D/I_G value of GO, TR and ZTR 3 composites are 0.81, 0.91 and 0.93, respectively. Compared with GO, the high I_D/I_G intensity ratios of TR and ZTR 3 composites indicate that the addition of TiO_2 and $ZnFe_2O_4$ increased the structural disorder of graphene.[33,34]

To further analyze the elemental components and chemical valence state, XPS measurement of ZTR 3 composite is investigated. Fig. 5a shows the elemental of C, Ti, O, Fe and Zn elements in ZTR 3 composite, which is consistent with experimental theoretical value. As displayed in Fig. 5b, the C 1s peaks can be divided into three different peaks located at 284.6 eV, 286.5 eV, and 288.3 eV, which are associated with C=C, C–O, and C=O coordination, respectively.[33] Fig. 5c displays the O 1s XPS spectrum, the peak of O 1s centered at the binding energy of 530.4 eV corresponds to the metal–oxygen bonds from the $ZnFe_2O_4$ and TiO_2.[35] While the peaks with the binding energies of 531.9 eV and 533.1 eV relate to oxygen bonded to contaminated carbon (C–O, C=O).[36] In Fig. 5d, it can be clearly observed that the Zn 2p spectrum shows peaks at 1021.5 eV and 1044.6 eV, which could be assigned to Zn $2p_{3/2}$ and Zn $2p_{1/2}$, respectively.[35] The Fe 2p spectrum in Fig. 5e can be fitted into two peaks, corresponding to the binding energies of Fe $2p_{3/2}$ (710.1 eV) and Fe $2p_{1/2}$ (724.8 eV), respectively. The Zn 2p and Fe 2p photoelectron peaks are consistent with the peaks reported for Zn^{2+} and Fe^{3+} in the $ZnFe_2O_4$.[34] The XPS spectrum of Ti 2p (Fig. 5f) shows two peaks at 458.8 eV and 464.6 eV, which are assigned to Ti $2p_{3/2}$ and Ti $2p_{1/2}$ of Ti^{4+} in anatase TiO_2, suggesting the valence of Ti is four.[37]

As we known, the fluorescence intensity of photocatalyst is positively correlated with the recombination rate of e^- and h^+ pairs.[38] In Fig. 6, we can see that all samples show a strong peak locate at 491 nm. When combined with RGO and $ZnFe_2O_4$, all

 This journal is © The Royal Society of Chemistry 2020

Open Access Article. Published on 05 May 2020. Downloaded on 2/8/2026 9:49:05 PM.
This article is licensed under a Creative Commons Attribution-NonCommercial 3.0 Unported Licence.

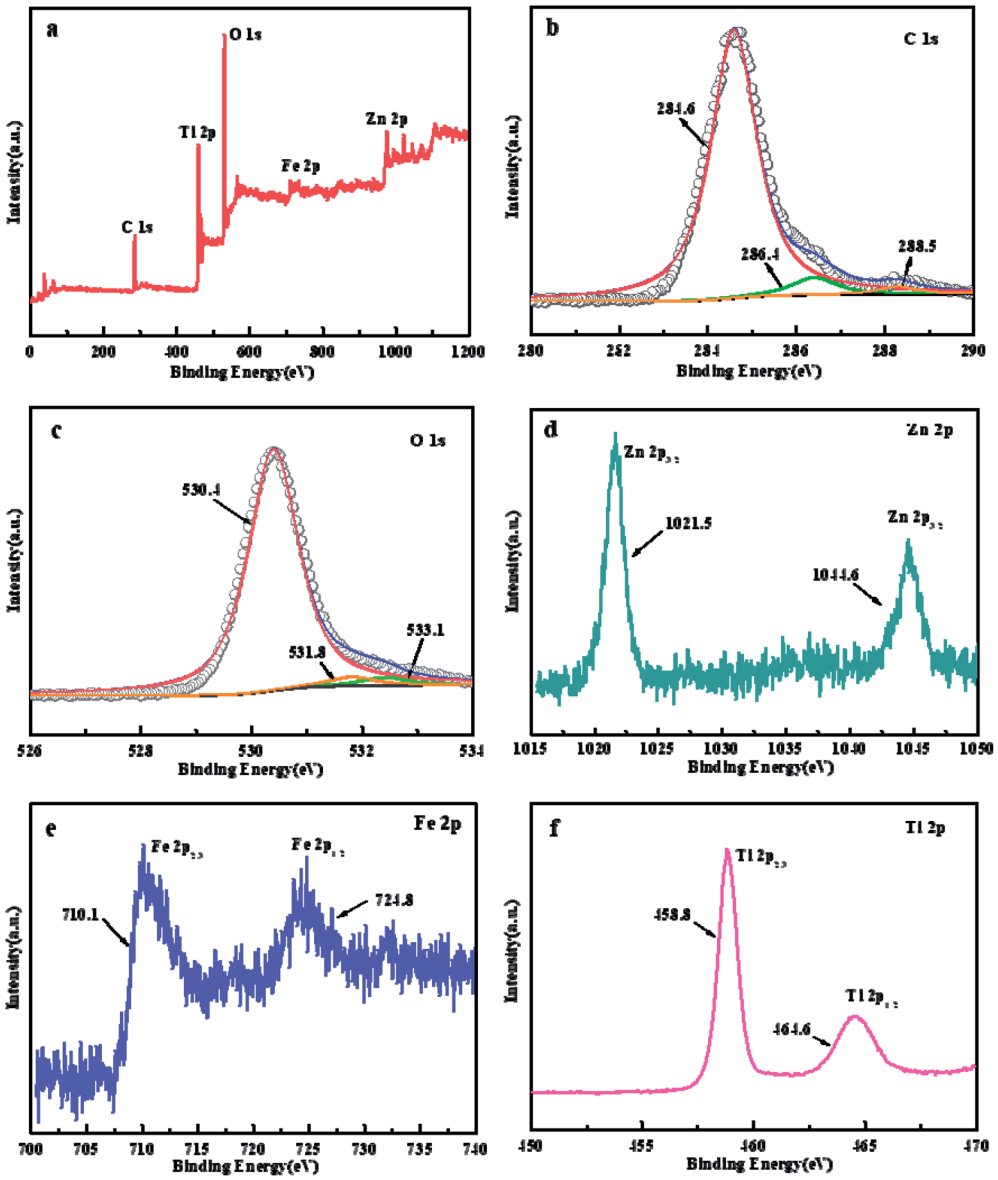

Fig. 5 XPS spectrum of (a) full spectra scan, (b) C 1s, (c) O 1s, (d) Zn 2p, (e) Fe 2p and (f) Ti 2p for ZTR 3 composite.

peaks of TR and ZTR 3 are decreased significantly. Compared with TiO_2 and TR, ZTR 3 composite has the lowest PL intensity, which indicates that the lowest e^- and h^+ pairs recombination rate and the strongest photocatalytic efficiency.[39]

3.2 Photocatalytic activity

Fig. 7a and c show that in the absence of photocatalysts, the concentration of *p*-NP almost unchanged on both simulated solar irradiation and visible light irradiation. However, the concentration of *p*-NP gradually decreases with the addition of photocatalysts. In dark reaction, the concentration of *p*-NP decreased after adding the photocatalysts, which due to the adsorption on the catalyst surface. With the increase of RGO ratio in the photocatalyst, the adsorption capacity of *p*-NP on the surface of photocatalyst is stronger. Compared with

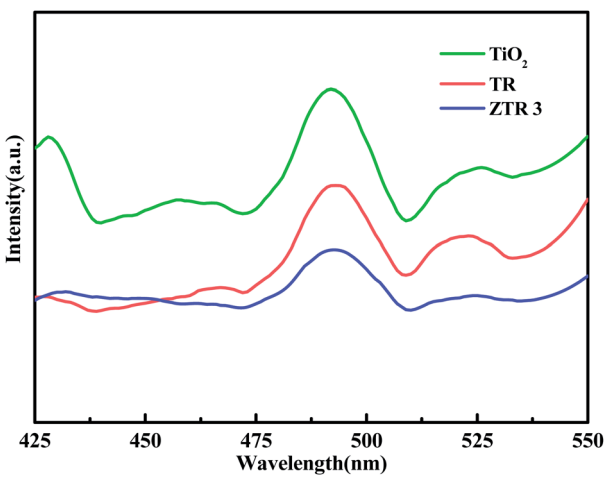

Fig. 6 The PL spectrum of TiO_2, TR and ZTR 3 composite (310 nm excitation light source).

Open Access Article. Published on 05 May 2020. Downloaded on 2/8/2026 9:49:05 PM.
This article is licensed under a Creative Commons Attribution-NonCommercial 3.0 Unported Licence.

$ZnFe_2O_4$ and TiO_2 nanosheets, TR shows the higher photocatalytic degradation efficiency for *p*-NP under both simulated solar irradiation (from 28.9% and 33.1% to 60% in 60 min) and visible light irradiation (from 23.5% and 22.1% to 53.7% in 80 min), which mainly attribute to the lower recombination rate of e^+ and h^- pairs in TR composite. In addition, the adsorption of *p*-NP on RGO is also benefit to the improvement of photocatalytic activity.[40] Furthermore, ZTR 1, ZTR 3 and ZTR 5 composites exhibit the enhanced photocatalytic activity than TR composite. When the percentage of RGO in composite reach from 3% to 5%, the photocatalytic degradation of *p*-NP decreases from 99.7% to 98.8% under simulated solar irradiation, the same trend is observed under visible light irradiation. This phenomenon may be due to higher black RGO contents may lead to a shield of the active sites on the photocatalyst surface sites.[33]

Fig. 7b and d show that the plots of $-\ln(C_t/C_0)$ *vs.* time are linear for all composites, confirming that the photodegradation of *p*-NP obeys pseudo first-order kinetics under simulated solar irradiation and visible light irradiation, respectively. The slope linear is apparent rate constant (k), which are calculated in Fig. 7e. The k values of the prepared composites are listed in Table 1. The fitting parameters reveal that reaction rate of ZTR 3 composite is faster than that of other composites, indicating it has an excellent photodegradation on *p*-NP pollutants.

The mineralization efficiency of *p*-NP was tested by total organic carbon (TOC) analysis. As seen in Fig. 7f, TOC degradation rates of *p*-NP are 87.6% and 75.3% in 300 min catalyzed by the ZTR 3 composite under simulated solar irradiation and

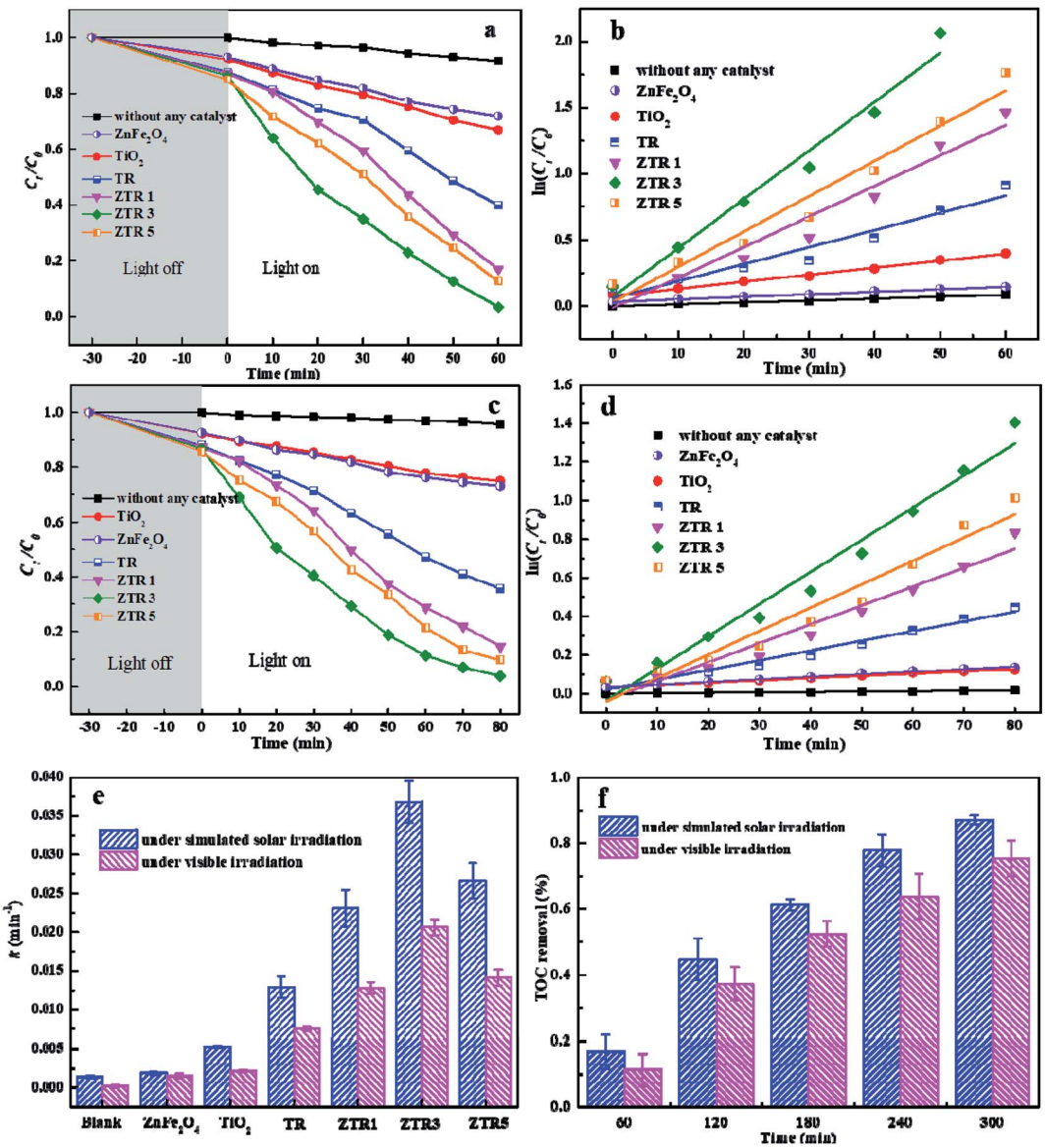

Fig. 7 (a and b) Photodegradation efficiency of prepared composites under simulated solar irradiation and the relationship between $-\ln(C_t/C_0)$ and time, (c and d) photodegradation efficiency of prepared composites under visible light irradiation and the relationship between $-\ln(C_t/C_0)$ and time, (e) first-order rate constant k values and (f) TOC changes of *p*-NP in presence of ZTR 3 composite.

 This journal is © The Royal Society of Chemistry 2020

Open Access Article. Published on 05 May 2020. Downloaded on 2/8/2026 9:49:05 PM.
This article is licensed under a Creative Commons Attribution-NonCommercial 3.0 Unported Licence.

Table 2 Summary and comparison of different photocatalysts

Photocatalyst	Light	Concentration	Time	Degradation	Ref.
W–TiO_2/SiO_2	UV light	25 mg L^{-1}	240 min	99%	41
ZnO–N/CF	UV light	20 mg L^{-1}	150 min	98%	42
$H_3PW_{12}O_{40}$/TiO_2–g-C_3N_4	Visible light	20 mg L^{-1}	120 min	98.6%	43
Sr^{2+}/Ag–TiO_2@rGO	Visible light	15 mg L^{-1}	180 min	99.9%	44
ZTR 3	UV-Vis light	10 mg L^{-1}	60 min	99.7%	This work
ZTR 3	Visible light	10 mg L^{-1}	80 min	99.6%	This work

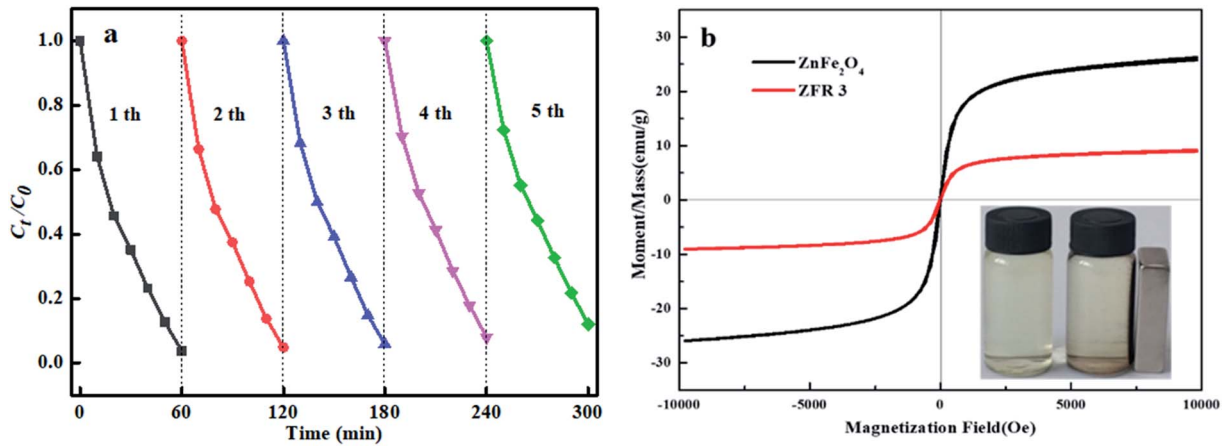

Fig. 8 (a) Reusability of ZTR 3 composite for five recycling runs and (b) magnetic hysteresis loops of $ZnFe_2O_4$ and ZTR 3 composites under an external magnetic field.

visible light irradiation, respectively. TOC concentration decrease from 6.86 mg L^{-1} to 0.85 mg L^{-1} and 1.69 mg L^{-1}. This means that most of organic carbon in *p*-NP change to inorganic carbon in the solution.

Table 2 lists the comparisons of photocatalytic efficiencies of the ZTR 3 composite with other nanocomposites reported for degradation of *p*-NP. ZTR 3 composite showed enhanced pollutant degradation efficiency of *p*-NP.

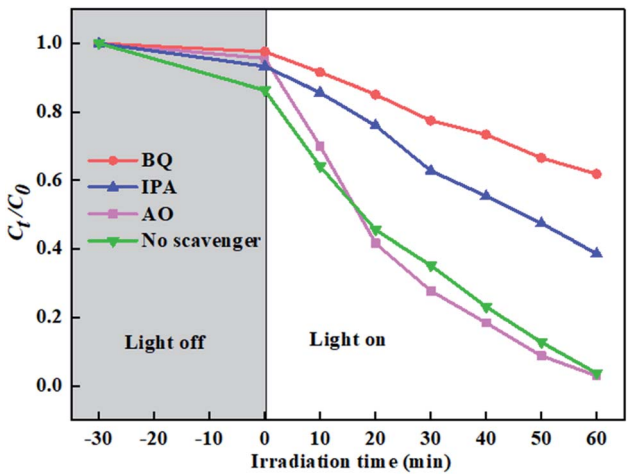

Fig. 9 Active species trapping experiments over ZTR 3 composite alone, and with addition of AO, IPA and BQ.

3.3 Reusability of the ZTR 3 composite

In Fig. 8a, the stability and reusability of ZTR 3 composite was researched by photodegradation of *p*-NP for 5 cycles. The photodegradation of *p*-NP decreases to 88.1% after five recycling runs, illustrating that ZTR 3 composite exhibits a relatively stable photocatalytic activity. Magnetic hysteresis loops of $ZnFe_2O_4$ and ZTR 3 composite displayed in Fig. 8b, which reveal that $ZnFe_2O_4$ and ZTR 3 composite equipped the magnetic material characteristic. The magnetic saturation (M_s) of $ZnFe_2O_4$ (26.2 emu g^{-1}) is higher than ZTR 3 (9.2 emu g^{-1}) composite, which may be attributed to a small proportion of $ZnFe_2O_4$ in ZTR 3 composite. The inset of Fig. 8b confirms that the ZTR 3 composite can be separated by an external magnetic field in *p*-NP solution.

3.4 Possible photocatalytic mechanism

The active species trapping experiments were investigated to analyze the photocatalytic mechanism of ZTR 3 composite. As shown in Fig. 9, when AO (a quencher of h^+) is added, the degradation rate of *p*-NP is slightly improved, which due to promotion of photogenerated e^-/h^+ pairs separation.[45] The degradation rates of *p*-NP decrease to 38.2% and 66.4% with addition of BQ (a quencher of $^{\bullet}O_2^-$) and IPA (a quencher of $^{\bullet}OH$), respectively. Therefore, we can draw a conclusion that $^{\bullet}O_2^-$ and $^{\bullet}OH$ are the main active species in photocatalytic degradation of *p*-NP by ZTR 3 composite.

Open Access Article. Published on 05 May 2020. Downloaded on 2/8/2026 9:49:05 PM.
This article is licensed under a Creative Commons Attribution-NonCommercial 3.0 Unported Licence.

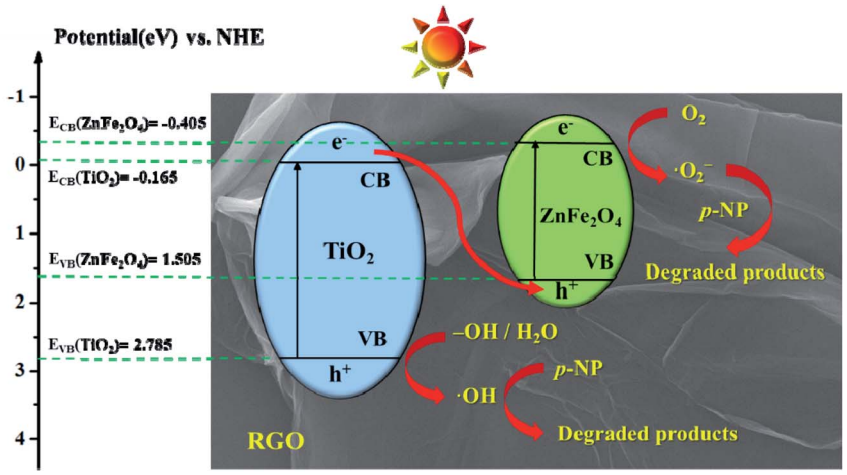

Fig. 10 Schematic illustration of possible photocatalytic mechanism of ZTR 3 composite under simulated solar irradiation.

According to formulas (2) and (3) (in SI), the calculated E_{VB} and E_{CB} of TiO_2 are 2.785 eV and −0.165 eV, and for control $ZnFe_2O_4$ they are 1.505 eV and −0.405 eV, respectively. Under the simulated solar irradiation, both TiO_2 and $ZnFe_2O_4$ can be excited to generate photogenerated e^- and h^+. However, the potential of the –OH/$^\cdot$OH and H_2O/$^\cdot$OH couples are 2.7 eV and 2.4 eV *vs.* NHE,[46] which locate lower than the VB of $ZnFe_2O_4$ (1.505 eV). This indicates that $ZnFe_2O_4$ cannot react with –OH/H_2O to produce $^\cdot$OH, which is not consistent with the trapping experiments. Thus, the photogenerated e^-/h^+ pairs of ZTR 3 composite form a Z-scheme photocatalytic system. As shown in Fig. 10, photogenerated h^+ still leave the VB of TiO_2, and the photogenerated e^- in TiO_2 migrate to VB of $ZnFe_2O_4$. The Z-scheme mechanism promote an efficient separation space between the photogenerated e^- and h^+.[21] As another main component in the ZTR 3 composite, RGO act as the receiver and transmitter of photogenerated e^-, which further reduce the recombination of e^- and h^+.[47] Accordingly, photogenerated h^+ in VB of TiO_2 oxidize the –OH or H_2O to $^\cdot$OH, and photogenerated e^- in CB of $ZnFe_2O_4$ react with O_2 to produce $^\cdot O_2^-$. Eventually, these highly active species degrade the *p*-NP.

4. Conclusions

A magnetic separable Z-scheme system of $ZnFe_2O_4/TiO_2$/RGO composite was successfully synthesized by one-step hydrothermal method. The ZTR 3 composite exhibited the highest *k* value (36.85×10^{-3} min^{-1}), which was 6.98 and 2.86 times higher than TiO_2 (5.28×10^{-3} min^{-1}) and TiO_2/RGO (12.89×10^{-3} min^{-1}). The photocatalytic degradation of *p*-NP reached to 99.7% under simulated solar irradiation within 60 min and the TOC degradation of *p*-NP was 87.6% in 300 min. Furthermore, 5 time cycles of photocatalytic experiments revealed an excellent stability and reusability of ZTR 3 composite. Finally, the excellent photocatalytic activity of ZTR 3 composite was mainly attributed to the rapid charge transfer of the Z-scheme system. In conclusion, the magnetic separable $ZnFe_2O_4/TiO_2$/RGO composite with an excellent photocatalytic efficiency displayed great prospects in the degradation of *p*-NP wastewater.

Conflicts of interest

There are no conflicts to declare.

Acknowledgements

This work was supported by the Development and Reform Commission of Jilin Province (No. 2015Y049), the National Natural Science Foundation of China (51708250), the Project of Department of Science and the Technology of Jilin Province (20180623042TC).

References

1 B. Boruah, R. Gupta, J. M. Modak and G. Madras, *J. Photochem. Photobiol., A*, 2019, **373**, 105–115.
2 N. San, A. Hatipoğlu, G. Koçtürk and Z. Çınar, *J. Photochem. Photobiol., A*, 2002, **146**, 189–197.
3 Y. L. Luo, W. S. Guo, H. H. Ngo, L. D. Nghiem, F. I. Hai, J. Zhang, S. Liang and X. C. C. Wang, A review on the occurrence of micropollutants in the aquatic environment and their fate and removal during wastewater treatment, *Sci. Total Environ.*, 2014, **473**, 619–641.
4 N. H. Tran, M. Reinhard and K. Y. H. Gin, Occurrence and fate of emerging contaminants in municipal wastewater treatment plants from different geographical regions-a review, *Water Res.*, 2018, **133**, 182–207.
5 K. Ravi, B. S. Mohan, R. B. Anjaneyulu, G. S. Sree and K. Basavaiah, *Phys. B*, 2019, **553**, 190–194.
6 Y. C. Wu, Z. M. Liu, Y. R. Li, J. T. Chen, X. X. Zhu and P. Na, *Chin. J. Catal.*, 2019, **40**, 60–69.
7 Z. Y. Jiang, X. Z. Liang and Y. Y. Liu, *Appl. Catal., B*, 2017, **211**, 252–257.
8 K. X. Wang, C. L. Shao and X. H. Li, *Materials*, 2016, **9**, 90.

 This journal is © The Royal Society of Chemistry 2020

Open Access Article. Published on 05 May 2020. Downloaded on 2/8/2026 9:49:05 PM.
This article is licensed under a Creative Commons Attribution-NonCommercial 3.0 Unported Licence.

9 J. Tian, Y. Sang, G. Yu, H. Jiang, X. Mu and H. Liu, *Adv. Mater.*, 2013, **25**, 5075–5080.
10 G. H. Moon, D. H. Kim and H. I. Kim, *Environ. Sci. Technol.*, 2014, **1**(2), 185–190.
11 Y. R Li, Z. M. Liu, Y. C. Wu, J. T. Chen, J. Y. Zhao, F. M. Jin and P. Na, *Appl. Catal., B*, 2018, **224**, 508–517.
12 K. Nakata, T. Ochiai, T. Murakami and A. Fujishima, *Electrochim. Acta*, 2012, **84**, 103–111.
13 H. Tong, S. X. Ouyang, Y. P. Bi, N. Umezawa, M. Oshikiri and J. H. Ye, *Adv. Mater.*, 2012, **24**, 229–251.
14 N. M. Gupta, S. Kelkar and P. Korake, *Photochem. Photobiol. Sci.*, 2016, **15**(6), 758–766.
15 N. K. Eswar, P. C. Ramamurthy and G. Madras, *Photochem. Photobiol. Sci.*, 2015, **14**, 1227–1237.
16 J. Q. Qin, X. Y. Zhang, C. W. Yang, M. Cao, M. Z. Ma and R. P. Liu, *Appl. Surf. Sci.*, 2017, **392**, 196–203.
17 S. Bellamkonda, N. Thangavel, H. Y. Hafeez, B. Neppolian and G. R. Rao, *Catal. Today*, 2017, **321–322**, 120–127.
18 H. Xu, M. M. Ding, W. Chen, Y. Li and K. Wang, *Sep. Purif. Technol.*, 2018, **195**, 70–82.
19 M. Faraldos and A. Bahamonde, *Catal. Today*, 2017, **285**, 13–28.
20 S. Y. Pu, R. X. Zhu, H. Ma, D. L. Deng, X. J. Pei, F. Qi and W. Chu, *Appl. Catal., B*, 2017, **218**, 208–219.
21 H. N. Che, C. B. Liu, W. Hu, H. Hu, J. Q. Li, J. Y. Dou, W. D. Shi, C. M. Li and H. J. Dong, *Catal. Sci. Technol.*, 2018, **8**, 622.
22 L. Zhu, X. Q. Kong, C. W. Yang, B. X. Ren and Q. Tang, *J. Hazard. Mater.*, 2020, **381**, 12910.
23 Y. F. Jia, J. Liu, S. W. Cha, S. Choi, Y. C. Park and C. L. Liu, *J. Ind. Eng. Chem.*, 2016, **47**, 303–314.
24 A. H. Mady, M. L. Baynosa, D. Tuma and J. J. Shim, *Appl. Catal., B*, 2017, **203**, 416–427.
25 X. D. Zhu, F. Zhang, M. J. Wang, J. J. Ding, S. Sun, J. Bao and C. Gao, *Appl. Surf. Sci.*, 2014, 83–89.
26 Y. H. Cao, Q. Y. Li, C. Li, J. L. Li and J. J. Yang, *Appl. Catal., B*, 2016, **198**, 378–388.
27 J. Q. Qin, X. Y. Zhang, C. W. Yang, M. Cao, M. Z. Ma and R. P. Liu, *Appl. Surf. Sci.*, 2017, **392**, 196–203.
28 X. D Tang, Z. R. Wang and Y. Wang, *Appl. Surf. Sci.*, 2018, **427**, 123–132.
29 X. L. Hu, S. C. Lu, J. Tian, N. Wei, X. J. Song, X. Z. Wang and H. Z. Cui, *Appl. Catal., B*, 2019, **241**, 329–337.
30 Y. S. Fu and X. Wang, *Ind. Eng. Chem. Res.*, 2011, **50**, 7210–7218.
31 T. Y. Liu, B. Liu, L. F. Yang, X. L. Ma, H. Li, S. Yin, T. Sato, T. Sekino and Y. H. Wang, *Appl. Catal., B*, 2017, **204**, 593–601.
32 Y. S. Fu, H. Q. Chen, X. Q. Sun and X. Wang, *AIChE J.*, 2012, **58**, 3298–3305.
33 H. Atout, M. G. Álvarez, D. Chebli, A. Bouguettoucha, D. Tichit, J. Llorca and F. Medina, *Mater. Res. Bull.*, 2017, **95**, 578–587.
34 S. Banerjee, P. Benjwal, M. Singh and K. K. Kar, *Appl. Surf. Sci.*, 2018, **439**, 560–568.
35 X. J. Chen, Y. Z. Dai and T. H. Liu, *Catal. Commun.*, 2015, **71**, 21–27.
36 Q. C. Chen and Q. S. Wu, *J. Hazard. Mater.*, 2015, **283**, 193–201.
37 X. F. Meng, Y. Zhuang, H. Tang and C. H. Lu, *J. Alloys Compd.*, 2018, **761**, 15–23.
38 M. J. Zhou, J. Z. Li, Z. F. Ye, C. C. Ma, H. Q. Wang, P. W. Huo, W. D. Shi and Y. S. Yan, *ACS Appl. Mater. Interfaces*, 2015, **7**, 28231.
39 Y. W. Sun, Q. Tang, T. Tian and C. L. Kang, *ChemistrySelect*, 2019, **4**, 9476–9482.
40 J. J. Zhang, X. Liu, T. Ye, G. P. Zheng, X. C. Zheng, P. Liu and X. X. Guan, *J. Alloys Compd.*, 2017, **698**, 819–827.
41 U. A. Sánchez, L. C. Chen, J. A. Wang, L. E. Noreña, M. Asomoza, S. Solis, X. L. Zhou, Y. Q. Song and J. Liu, *Int. J. Photoenergy*, 2019, 5748586.
42 J. A. Allen, D. Murugesan and C. Viswanathan, *Superlattices Microstruct.*, 2019, **125**, 159–167.
43 L. J. Li, L. Li, T. T. Sun, X. M. Yu, L. Long, L. Xu and J. H. Yan, *J. Solid State Chem.*, 2019, **274**, 152–161.
44 X. Wei, J. Cao and F. Fang, *RSC Adv.*, 2018, **8**, 31822–31829.
45 J. G. Yu, S. H. Wang, J. X. Low and W. Xiao, *Phys. Chem. Chem. Phys.*, 2013, **15**, 16883–16890.
46 J. H. Lia, Y. L. Liu, H. M. Li and C. Chen, *J. Photochem. Photobiol., A*, 2016, **317**, 151–160.
47 H. Safajou, H. Khojasteh, M. S. Niasari and S. M. Derazkola, *J. Colloid Interface Sci.*, 2017, **498**, 423–432.